Theoretical Modeling and Experimental Verification of the Acceleration Factor for Narrow-Band Random Vibration Fatigue Tests.

LI, P, YAO, W, SUSMEL, Luca <http://orcid.org/0000-0001-7753-9176> and YIN, H

Theoretical Modeling and Experimental Verification of the Acceleration Factor for Narrow-Band Random Vibration Fatigue Tests

Piao Li [a,b*], Weixing Yao [c], Luca Susmel [d,*], Haibiao Yin [e]

[a]*Smart Materials and Advanced Structures Laboratory, School of Mechanical Engineering and Mechanics, Ningbo University, Ningbo 315211, China*

[b]*Jiangsu Province Key Laboratory of Aerospace Power System, Nanjing University of Aeronautics and Astronautics, Nanjing 210016, China*

[c]*Jiangsu Xinyang New Materials Co., Ltd., Yangzhou 225127, China*

[d]*School of Engineering and Built Environment, Sheffield Hallam University, Harmer Building, Sheffield S1 1WB, UK*

[e]*College of Aerospace Engineering, Nanjing University of Aeronautics and Astronautics, Nanjing 210016, China*

Abstract

In conventional vibration fatigue acceleration testing, the two-parameter S–N curve is widely used. However, its inability to accurately characterize the fatigue properties in high-cycle regime introduces intrinsic bias in long-term life prediction, particularly for vibration fatigue dominated by high-cycle failure. To improve physical accuracy, this study focuses on narrow-band random vibration and introduces a three-parameter S–N curve to better capture high-cycle fatigue properties. Based on this, a high-precision analytical model for the vibration fatigue acceleration factor is developed, and a closed-form solution in a generalized inverse power-law form is derived. Experimental validation is performed through vibration fatigue tests on Selective Laser Melting (SLM) aluminum and titanium alloys. The results show that when significant differences exist between two- and three-parameter S–N curves, the three-parameter model significantly improves prediction accuracy of the vibration fatigue acceleration factor, confirming the necessity and effectiveness of this study.

Key words：Fatigue, Random vibration, S-N curve, Acceleration factor, Narrow-band

1. Introduction

In engineering fields such as aerospace, high-speed rail transit, and wind power generation, structural components are often subjected to severe random vibration environments, making vibration fatigue one of the primary failure modes. Since the actual service life of such structures typically extends to millions or even hundreds of millions of load cycles, conducting full-lifetime tests under real loading conditions poses formidable challenges due to the extremely long testing duration and high associated costs. Consequently, accelerated vibration fatigue testing techniques have emerged as an effective solution. Their core objective is to reduce testing time, enhance testing efficiency, and lower costs through rational theoretical frameworks and

* Corresponding author.
Piao Li, Email: lipiao@nuaa.edu.cn
Luca Susmel, Email: l.susmel@shu.ac.uk

methodologies, thereby enabling the acquisition of vibration fatigue characteristics of structures within a shorter time frame and at a lower expense.

At present, most industrial applications follow established standards such as ISO 16750-3 (Automotive Environmental Conditions and Testing for Electrical and Electronic Equipment), IEC 61373 (Railway Applications - Rolling stock equipment - Shock and vibration tests), and the U.S. military standard MIL-STD-810G [1] for conducting accelerated tests. These standards are fundamentally derived from the inverse power-law model of fatigue acceleration testing [2].

Accelerated fatigue testing methods have been the subject of extensive research. From a methodological perspective, accelerated vibration fatigue techniques can generally be categorized into time-domain, frequency-domain, and hybrid approaches. Time-domain methods directly manipulate load histories by reconstructing stress–time signals and applying fatigue load spectrum editing techniques. As reviewed by Farrar et al. [3], these approaches aim to improve testing efficiency by increasing loading frequency or eliminating low-damage cycles. They are also commonly referred to as fatigue load spectrum editing. In practice, the response stress or strain spectrum at critical structural locations is first obtained through measurement or numerical simulation. The stress–time history is then reconstructed using rainflow counting, followed by various editing operations—including acceleration, deletion, equivalent combination, and amplification—to generate a peak–valley load sequence for accelerated testing. Time-domain acceleration methods can significantly reduce the duration of load time histories and offer a more quantitative and precise framework. Subsequent studies have demonstrated their applicability in both numerical and experimental contexts. For example, Xu et al. [4] investigated fatigue acceleration through load spectrum editing combined with finite element simulations, while Ameur et al. [5] extended such approaches to composite materials under random vibration. More recently, Dupke et al. [6] developed a high-frequency vibration-based fatigue testing method, showing consistency with conventional low-frequency fatigue results. Despite their clear physical interpretability, time-domain methods rely heavily on empirical operations and involve significant computational and experimental effort, which limits their practical application. In addition, the validity of acceleration depends entirely on the adopted damage accumulation model and the accuracy of the material S–N curve. If the underlying model contains inherent deficiencies—such as neglecting the fatigue limit—systematic bias may be introduced into the accelerated test results. Moreover, pursuing extremely high acceleration factors by excessively compressing test duration often comes at the expense of damage simulation fidelity. The complexity of load time histories further limits the practical applicability of time-domain acceleration methods.

As a result, frequency-domain approaches have become the dominant strategy in accelerated vibration fatigue research. These methods typically achieve acceleration via two strategies: (i) increasing the excitation level while keeping the frequency band unchanged, or (ii) modifying the frequency band of random vibration excitation while maintaining a constant excitation level. A combination of both strategies is also possible, although the former approach is more commonly adopted in practice. Within this framework, Allegri [7] proposed an inverse power-law model based on the equivalent von Mises stress criterion, which was further analyzed and validated by Benasciutti [8]. Experimental investigations have also been conducted under various excitation conditions, including sinusoidal, random, and resonant loading [9]. Extensions to non-Gaussian

random vibration environments [10], step-loading strategies [11], and high-kurtosis excitation signals [12] have significantly enhanced testing efficiency. Additional studies have explored simplified excitation strategies [13], spectrum reconstruction methods based on segmented S–N curves [14], and acceleration factor formulations derived from power spectral density functions [15], while the influence of damping effects has also been examined [16]. These developments have greatly improved the applicability of frequency-domain methods for simulating fatigue damage under realistic vibration conditions.

In recent years, hybrid or synthesis-based approaches have attracted increasing attention. For instance, mission synthesis-based methods have been proposed to tailor accelerated test profiles [17], while power-density-based load spectrum editing techniques have been developed to preserve key characteristics of operational loads [18]. Furthermore, integrated frameworks combining multibody dynamics, finite element analysis, and experimental measurements have been successfully applied to engineering systems [19]. Advances have also been made in multiaxial vibration fatigue testing [20] and calibrated accelerated life testing methodologies for structural components [21]. These hybrid approaches aim to improve both the realism and efficiency of accelerated fatigue testing.

Despite these significant advancements, a fundamental issue remains insufficiently addressed. Vibration fatigue is inherently governed by high-cycle and very-high-cycle fatigue behavior. However, most existing models rely on two-parameter S–N curves, which neglect the fatigue limit and therefore fail to accurately describe material behavior in the high-cycle regime. This limitation may introduce systematic bias into fatigue life predictions, particularly under random vibration conditions where the stress response follows a distribution rather than a single deterministic value. To address this gap, the present study aims to develop a high-accuracy analytical model for the vibration fatigue acceleration factor based on a three-parameter S–N curve. First, the general characteristics of S–N relationships for engineering materials are discussed, and a three-parameter formulation is adopted to more accurately capture fatigue behavior, particularly in the high-cycle regime. Subsequently, a closed-form analytical expression for the acceleration factor under narrow-band random vibration is derived. Finally, experimental validation is performed through vibration fatigue tests on Selective Laser Melting (SLM) aluminum and titanium alloys, and the theoretical predictions are systematically compared with experimental results to demonstrate the validity and accuracy of the proposed model.

2. Acceleration Factor Model

The fundamental principle of vibration fatigue acceleration testing is the concept of “equal damage”, in which the damage evaluation is based on the material’s fatigue S–N curve, and damage accumulation is typically described by Miner’s linear damage rule. The basic idea of the accelerated test is to intensify the excitation spectrum, so that the critical locations of the structure experience higher stress and strain levels, thereby achieving a substantial reduction in testing time. The degree of reduction is quantified by the acceleration factor η, which is defined as the ratio between the fatigue life under the original excitation spectrum T_0 and that under the accelerated excitation spectrum T, i.e., $\eta = T_0/T$.

Consider a structure subjected to a random vibration excitation spectrum $G(f)$. Through structural dynamic analysis or experiments, the stress response power spectral density (PSD) at the critical location can be obtained as $G_S(\omega)$, and the corresponding stress amplitude probability density function (PDF) as $p(S)$.

Under the narrow-band assumption, the stress amplitude distribution $p(S)$ follows a Rayleigh distribution [22],

$$p(S)=\frac{S}{\sigma_{\mathrm{RMS}}^2}\exp\left(-\frac{S^2}{2\sigma_{\mathrm{RMS}}^2}\right) \tag{1}$$

where σ_{RMS} denotes the root mean square (RMS) value of stress. The fatigue damage D at this critical point can then be expressed as [23]:

$$D=\nu T\int_0^{\infty}\frac{p(S)}{N(S)}\mathrm{d}S \tag{2}$$

where $N(S)$ represents the material's S–N curve, T is the vibration fatigue duration, and $\nu=\frac{1}{2\pi}\sqrt{\frac{m_2}{m_0}}$ denotes the mean vibration frequency, which is determined from the spectral moments m_i of the stress response power spectral density $G_{\mathrm{S}}(\omega)$, calculated as:

$$m_i=\int_0^{\infty}\omega^i G_{\mathrm{S}}(\omega)\mathrm{d}\omega \tag{3}$$

The RMS value of the stress for the random process is $\sigma_{\mathrm{RMS}}=\sqrt{m_0}$, and the bandwidth coefficient is denoted as $\varepsilon=\sqrt{1-\frac{m_1^2}{m_0 m_2}}$.

Assume that the original excitation PSD is $G_0(f)$, and the accelerated excitation PSD is $G_1(f)$. When both spectra act on the same structure, the corresponding stress response PSDs are $G_{\mathrm{S0}}(\omega)$ and $G_{\mathrm{S1}}(\omega)$, respectively. From these, the associated stress amplitude PDFs $p_0(S)$ and $p_1(S)$ can be obtained, and the resulting fatigue damages D_0 and D_1 are expressed as:

$$\begin{aligned}D_0&=\nu_0 T_0\int_0^{\infty}\frac{p_0(S)}{N(S)}\mathrm{d}S\\ D_1&=\nu_1 T_1\int_0^{\infty}\frac{p_1(S)}{N(S)}\mathrm{d}S\end{aligned} \tag{4}$$

The condition for conducting an accelerated fatigue life test is equal damage, i.e., $D_0=D_1$. From Eq. (4),

$$\nu_0 T_0\int_0^{\infty}\frac{p_0(S)}{N(S)}\mathrm{d}S=\nu_1 T_1\int_0^{\infty}\frac{p_1(S)}{N(S)}\mathrm{d}S \tag{5}$$

Since the same structure is considered, its inherent dynamic characteristics remain unchanged under different random vibration excitations, therefore, $\nu_0=\nu_1$. Accordingly, the acceleration factor η can be defined as

$$\eta=\frac{T_0}{T_1}=\frac{\int_0^{\infty}\frac{p_1(S)}{N(S)}\mathrm{d}S}{\int_0^{\infty}\frac{p_0(S)}{N(S)}\mathrm{d}S} \tag{6}$$

Eq.(6) provides the general expression of the acceleration factor η, which involves both the bandwidth characteristics of the random vibration and the form of the material's S–N curve.

The experimental data of the material's S–N curve usually exhibit an S-shaped trend [23]. Fig.1 shows the S–N curve of SLM-manufactured aluminum alloys as an example. Numerous mathematical formulations have

been proposed to describe the S–N relationship. Among them, two types of S–N curves are widely adopted in engineering applications: the two-parameter power function and the three-parameter power function.

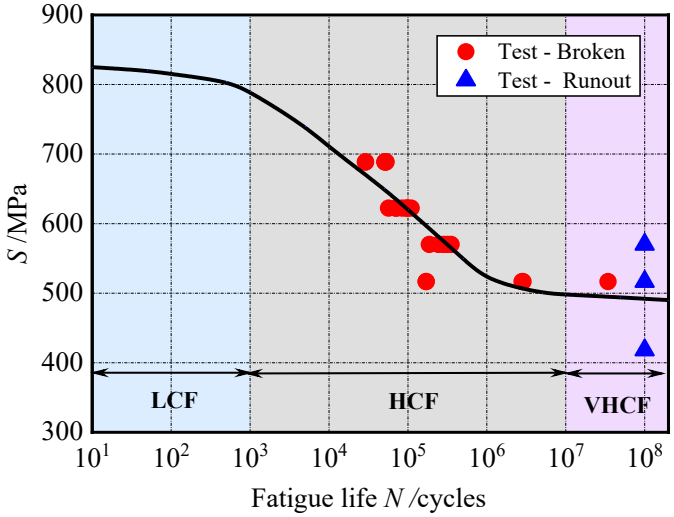

Fig.1 An example S-N curve of SLM-manufactured aluminum alloys

For single low-cycle fatigue (LCF) / high-cycle fatigue (HCF) / very-high-cycle fatigue (VHCF) regime, the two-parameter power-law form of the S–N curve is commonly used in both research and engineering practice. It can be expressed as:

$$S^{b_0} N = C_0 \tag{7}$$

where b_0 and C_0 are exponent and constant of the two-parameter S-N curve, respectively. Substituting Eqs. (1) and (7) into Eq. (6) yields

$$\begin{aligned} \eta &= \frac{\frac{b_0}{2}\left(\sqrt{2}\sigma_{\mathrm{RMS},1}\right)^{b_0}\Gamma\left(1+\frac{b_0}{2}\right)}{\frac{b_0}{2}\left(\sqrt{2}\sigma_{\mathrm{RMS},0}\right)^{b_0}\Gamma\left(1+\frac{b_0}{2}\right)} \\ &= \left(\frac{\sigma_{\mathrm{RMS},1}}{\sigma_{\mathrm{RMS},0}}\right)^{b_0} \end{aligned} \tag{8}$$

where $\sigma_{\mathrm{RMS},0}$ and $\sigma_{\mathrm{RMS},1}$ denote the RMS values of the response stress at the structural critical location under the original and accelerated excitation spectra, respectively. Eq. (8) thus represents the well-known inverse power-law model.

Since the vibration stress response of structures is typically at low or moderate levels—corresponding to the HCF and VHCF regions of the S–N curve—the three-parameter power-law S–N curve is more suitable and widely used in engineering applications. It can be expressed as:

$$N(S - S_{\mathrm{e}})^b = C \tag{9}$$

where S_{e} is the theoretical fatigue limit, and b and C are the exponent and constant of the three-parameter S–N curve, respectively. Substituting Eq. (9) into Eq. (6) gives

$$\eta = \frac{\frac{1}{C}\int_0^{\infty}(S - S_e)^b p_1(S)\mathrm{d}S}{\frac{1}{C}\int_0^{\infty}(S - S_e)^b p_0(S)\mathrm{d}S} \tag{10}$$

According to the generalized first mean-value theorem of integration, and noting that $p_0(S)$ and $p_1(S)$ are probability density functions, Eq (10) can be rewritten as

$$\eta = \frac{(S_1 - S_e)^b \int_0^{\infty} p_1(S)\mathrm{d}S}{(S_0 - S_e)^b \int_0^{\infty} p_0(S)\mathrm{d}S} = \frac{(S_1 - S_e)^b}{(S_0 - S_e)^b} \tag{11}$$

where S_0 and S_1 take certain values in (S_e, S_b). Assuming $S_i = S_e + \alpha_i(S_b - S_e), (i = 0,1)$, where S_b represents the ultimate tensile strength of the material, α is defined as the size factor, whose geometric meaning is illustrated in Fig.2.

$$\alpha_i = \frac{S_i - S_e}{S_b - S_e}, (i = 0,1) \tag{12}$$

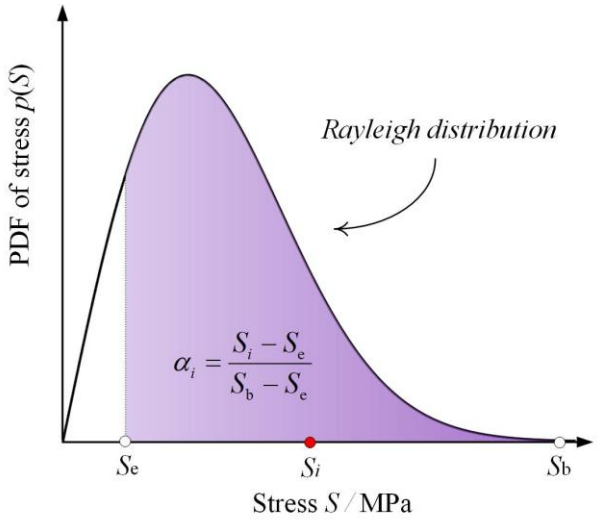

Fig2. Definition of size factor

Substituting Eq. (12) into Eq. (11) yields

$$\eta = \frac{(\alpha_1(S_b - S_e))^b}{(\alpha_0(S_b - S_e))^b} = \left(\frac{\alpha_1}{\alpha_0}\right)^b \tag{13}$$

The size factor α (α_0 or α_1) is related to the exponent *b* of the material's S–N curve and the probability density function *p*(*S*) of the response stress amplitude distribution. Since *b* is a material constant and independent of the excitation load, the size factor *α* depends solely on the excitation spectrum. Based on Eqs. (10)-(12), the size factor $\alpha(\alpha_0$ or $\alpha_1)$ can be expressed as

$$\alpha^b (S_b - S_e)^b = \int_0^{\infty}(S - S_e)^b p(S)\mathrm{d}S \tag{14}$$

Eq. (14) can be rewritten as

$$\alpha^b = \int_0^{\infty}\left(\frac{S - S_e}{S_b - S_e}\right)^b p(S)\mathrm{d}S \tag{15}$$

For an arbitrary b>0, Eq. (15) does not have an analytical solution. However, when b is a positive integer, Eq. (15) can be analytically solved to obtain a closed-form expression.

First, substituting Eq. (1) into Eq. (15) gives

$$\alpha^b = \int_0^{\infty} \left(\frac{S - S_{\mathrm{e}}}{S_{\mathrm{b}} - S_{\mathrm{e}}} \right)^b \left(\frac{S}{\sigma_{\mathrm{RMS}}^2} \right) \exp\left(-\frac{S^2}{2\sigma_{\mathrm{RMS}}^2} \right) \mathrm{d}S \tag{16}$$

By using the variable substitution method, $x = \dfrac{S^2}{2\sigma_{\mathrm{RMS}}^2}$, one obtains $S\mathrm{d}S = \sigma_{\mathrm{RMS}}^2 \mathrm{d}x$ and $S = \sigma_{\mathrm{RMS}} \sqrt{2x}$, and letting $\phi = (\sqrt{2}\,\sigma_{\mathrm{RMS}})/S_{\mathrm{e}}$ represents the level of vibration response stress, typically ranging from 1 to 5. Let $\psi = S_{\mathrm{b}}/S_{\mathrm{e}}$ denotes the fatigue performance of the material. Eq.(16) can then be written as

$$\begin{aligned} \alpha^b &= \int_0^{\infty} \left(\frac{\phi\sqrt{x} - 1}{\psi - 1} \right)^b \exp(-x)\,\mathrm{d}x \\ &= \frac{1}{(\psi - 1)^b} \int_0^{\infty} (\phi\sqrt{x} - 1)^b \exp(-x)\mathrm{d}x \\ &= \frac{1}{(\psi - 1)^b} \cdot I \end{aligned} \tag{17}$$

where the integral is $I = \int_0^{\infty} (\phi\sqrt{x} - 1)^b \exp(-x)\mathrm{d}x$. When b is a positive integer, the analytical solution of I is

$$\begin{aligned} I &= \int_0^{\infty} (\phi\sqrt{x} - 1)^b \exp(-x)\mathrm{d}x \\ &= \int_0^{\infty} \left(\sum_{k=0}^{b} C_b^k (-1)^k \phi^{b-k} x^{0.5(b-k)} \right) \exp(-x)\mathrm{d}x \\ &= \sum_{k=0}^{b} C_b^k (-1)^k \phi^{b-k} \left(\int_0^{\infty} x^{0.5(b-k)} \exp(-x)\mathrm{d}x \right) \\ &= \sum_{k=0}^{b} C_b^k (-1)^k \phi^{b-k} \Gamma\left(1 + (b-k)/2\right) \end{aligned} \tag{18}$$

in which $C_b^k = \dfrac{b!}{k!(b-k)!}$ is the binomial coefficient, b and k are positive integers, and $0 \le k \le b$. $\Gamma(\cdot)$ denotes the Gamma function, satisfying $\Gamma(1+x) = \int_0^{\infty} u^x \exp(-u)\mathrm{d}u$, and $\Gamma(1) = \Gamma(2) = 1$, $\Gamma(0.5) = \sqrt{\pi}$, $\Gamma(1+x) = x\Gamma(x)$, $\Gamma(1+n) = n!$.

Fig.3 shows the integral values and fitted expressions of Eq. (18) for b=2,3,…,10 and $\phi \in [1,5]$. The integral values I and ϕ under different b values can be well fitted by exponential functions, with fitting coefficients of determination R^2>0.995.

$$I = \lambda(b)\phi^{\kappa(b)} \tag{19}$$

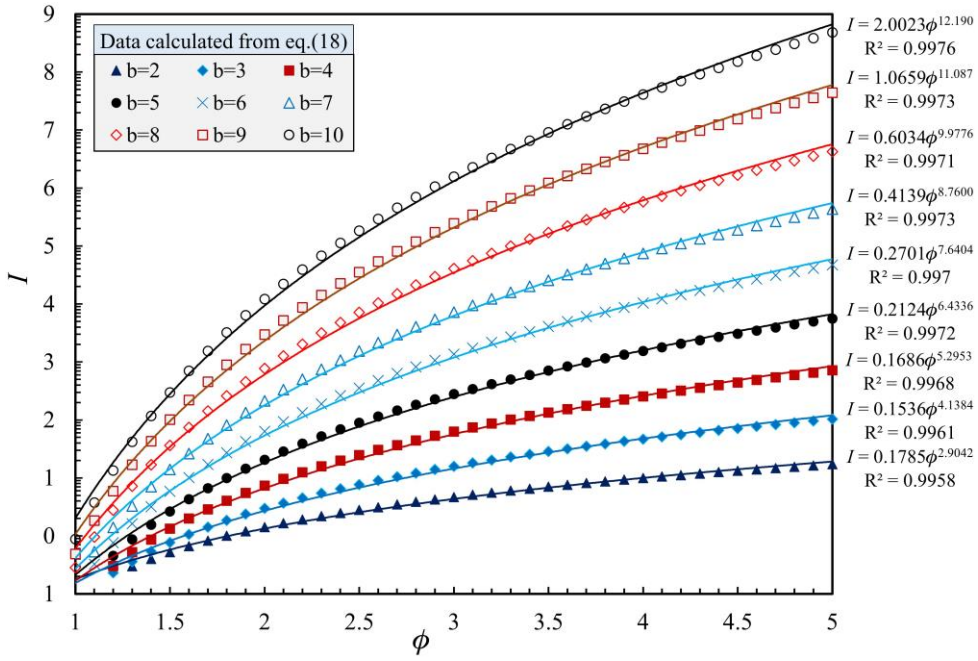

Fig.3 Integral value and fitting of Eq. (18)

The coefficients $\lambda(b)$ and exponents $\kappa(b)$ can be expressed as

$$\lambda(b) = 0.0098b^3 - 0.1259b^2 + 0.5165b - 0.4720$$
$$\kappa(b) = 1.1608b + 0.6418 \tag{20}$$

The fitting performance of Eq. (20) is shown in Fig.4, where the exponent $\kappa(b)$ exhibits a R^2=0.9999, and the coefficient $\lambda(b)$ yields R^2=0.9914.

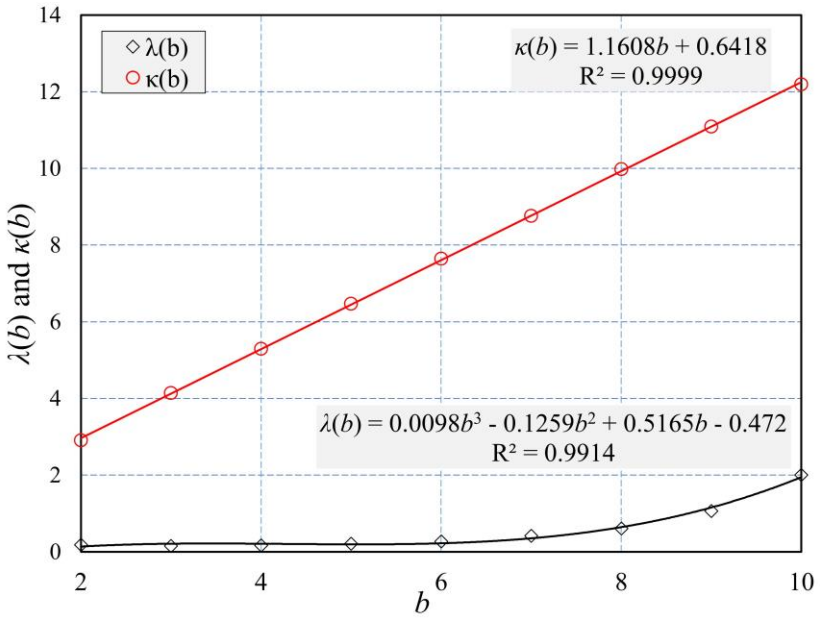

Fig.4 Fitted coefficients and exponents

Substituting Eq. (19) into Eq. (17), the empirical expression for α (α_0 or α_1) can be obtained.

$$\begin{aligned}\alpha^b &= \frac{1}{(\psi-1)^b}\cdot\lambda(b)\phi^{\kappa(b)} \\ &= \frac{1}{(S_\mathrm{b}/S_\mathrm{e}-1)^b}\cdot\lambda(b)\left(\frac{\sqrt{2}\sigma_\mathrm{RMS}}{S_\mathrm{e}}\right)^{\kappa(b)}\end{aligned} \tag{21}$$

Further substituting Eq. (21) into Eq. (13) yields the expression for the acceleration factor:

$$\begin{aligned}\eta &= \frac{\dfrac{1}{(S_\mathrm{b}/S_\mathrm{e}-1)^b}\cdot\lambda(b)\left(\dfrac{\sqrt{2}\sigma_{\mathrm{RMS},1}}{S_\mathrm{e}}\right)^{\kappa(b)}}{\dfrac{1}{(S_\mathrm{b}/S_\mathrm{e}-1)^b}\cdot\lambda(b)\left(\dfrac{\sqrt{2}\sigma_{\mathrm{RMS},0}}{S_\mathrm{e}}\right)^{\kappa(b)}} \\ &= \left(\frac{\sigma_{\mathrm{RMS},1}}{\sigma_{\mathrm{RMS},0}}\right)^{\kappa(b)} = \left(\frac{\sigma_{\mathrm{RMS},1}}{\sigma_{\mathrm{RMS},0}}\right)^{(0.6418+1.1608b)}\end{aligned} \tag{22}$$

By comparing Eq. (22) with Eq. (8), it can be observed that the two equations share the same mathematical form, and the expression of Eq.(22) can still be referred to as the generalized inverse power-law model, except that its exponent $\kappa(b)$ is now a function of the three-parameter S–N curve exponent *b*.

3. Experimental Validation

In this study, narrow-band random vibration accelerated fatigue tests were conducted on selective laser melting (SLM) fabricated high-strength Aluminum alloy TiB_2 and titanium alloy TC4 specimens to experimentally validate the proposed theoretical model.

3.1 Materials and specimens

The test specimens were manufactured from SLM high-strength Aluminum alloys (TiB_2) and titanium alloys (TC4). The chemical compositions of the two materials are listed in Tables 1(a) and 1(b), respectively, while their basic mechanical properties are summarized in Table 2.

Table 1(a) Chemical composition (wt%) of TiB_2

Elements	Al	Si	Ti	Mg	B	Fe	O	Zn	Cu	N	Mn	Ni
TiB_2	Bal.	10.09	0.69	0.44	0.32	0.085	0.0436	0.012	0.006	0.0032	0.002	0.002

Table 1(b) Chemical composition (wt%) of TC4

Elements	Ti	Al	V	Fe	O	N	C	H
TC4	Bal.	6.40	4.09	0.13	0.098	0.010	0.009	0.0033

Table 2 Static mechanical properties of experimental materials

Properties	Elastic modulus *E*/GPa	Poisson ratio ν	Density ρ / kg·m^{-3}	Ultimate strength σ_b/MPa
TiB_2	75.50	0.33	2644.003	440.08
TC4	112.00	0.34	4343.720	953.52

The S–N curve data of SLM TiB_2 and SLM TC4 are presented in Fig. 5, Eqs. (23) and (24). These data were obtained experimentally by the authors in a series of studies on the vibration fatigue behavior of SLM materials. Considering the limited scope of this paper and to avoid deviation from its central focus, the

experimental procedures are omitted, and only the results are reported herein.

$$\text{Two-parameter S-N curves} \quad \begin{matrix} \text{TiB}_2 & \log N = 17.359 - 6.152 \log S \\ \text{TC4} & \log N = 31.17 - 9.43 \log S \end{matrix} \tag{23}$$

$$\text{Three-parameter S-N curves} \quad \begin{matrix} \text{TiB}_2 & \log N = 16.77 - 4.87 \log(S - 17.30) \\ \text{TC4} & \log N = 16.58 - 4.68 \log(S - 293.23) \end{matrix} \tag{24}$$

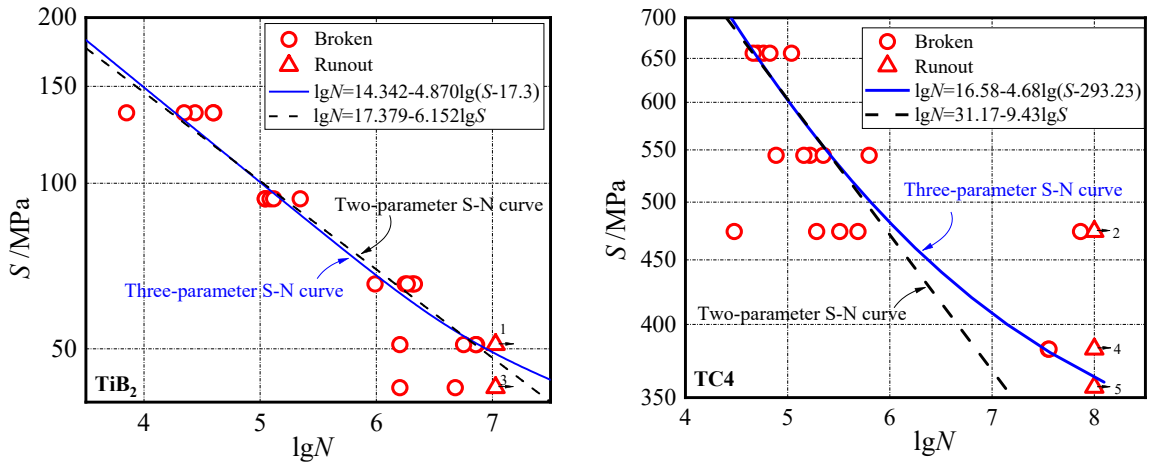

Fig.5 S-N curves of the tested materials

The geometry and dimensions of the specimens are illustrated in Fig. 6(a). Each specimen has an overall length of 80 mm and a thickness of 3 mm. The left end is the clamped section, featuring a clamping hole with a diameter of 8.2 mm. The transition section has a fillet radius of 25 mm. A counterweight hole with a diameter of 6.2 mm is located at the right end, where a counterweight of mass G=0.268 kg was attached during testing. A total of 30 TiB_2 specimens and 28 TC4 specimens were tested, labeled as TB-# and TC-#, respectively.

Prior to the vibration fatigue tests, a strain gauge was bonded along the central axis of each specimen, as shown in Fig. 6(b). The center of the strain gauge was aligned with the end of the variable cross-section region. During vibration loading, the strain response at this fixed location was continuously monitored to obtain the corresponding stress-time histories. The experimentally measured stress values were subsequently compared with those obtained from finite element analysis (FEA).

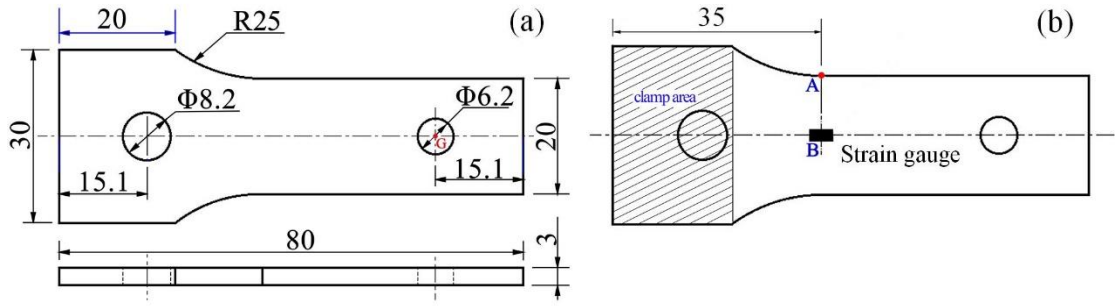

Materials	No.	Quantity
TiB_2	TB-#	30
TC4	TC-#	28

Fig.6 Specimen setup

To accurately characterize the structural dynamic properties of the SLM-fabricated specimens, modal

tests were performed using a high-precision sine sweep excitation method. In this procedure, a sinusoidal excitation with continuously varying frequency was applied to the specimen using an electrodynamic shaker, while the dynamic response was synchronously measured. By analyzing the excitation and response signals, key modal parameters—including natural frequencies, damping ratios, and mode shapes—were identified. The measured natural frequencies of the specimens are listed in Table 3.

Table 3 Tested dynamic characteristics of the specimen

Specimen	TB-1	TC-1
First-order natural frequency/Hz	72.12	93.62
Damping ratio ζ_1/%	1.401	1.350

3.2 Vibration Fatigue Tests

(1) Test Procedure

The base excitation spectrum was a narrow-band flat spectrum, as shown in Fig. 7. The excitation level m of each loading spectrum is listed in Table 4, where f_L and f_U denote the start and end frequencies, respectively, and # represents the spectrum sequence number.

Table 4 Baseline excitation spectrum

Spectrum No.	f_L /Hz	f_U /Hz	m / $(g^2 \cdot \mathrm{Hz}^{-1})$		
STB-#	64	81	0.05	0.10	0.20
STC-#	83	105	0.60	0.80	1.00

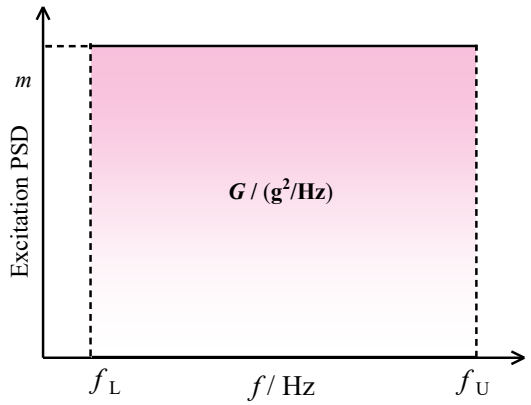

Fig.7 Vibration fatigue test load spectrum

The strain gauges were sticked onto the specimens, and the specimens were connected to the strain acquisition system and mounted on a SuShi DC-300-3 electrodynamic shaker, as shown in Fig.8. The vibration fatigue tests were then initiated. The test was terminated when either specimen fracture occurred or the natural frequency decreased by 10%, and the corresponding vibration fatigue life was recorded.

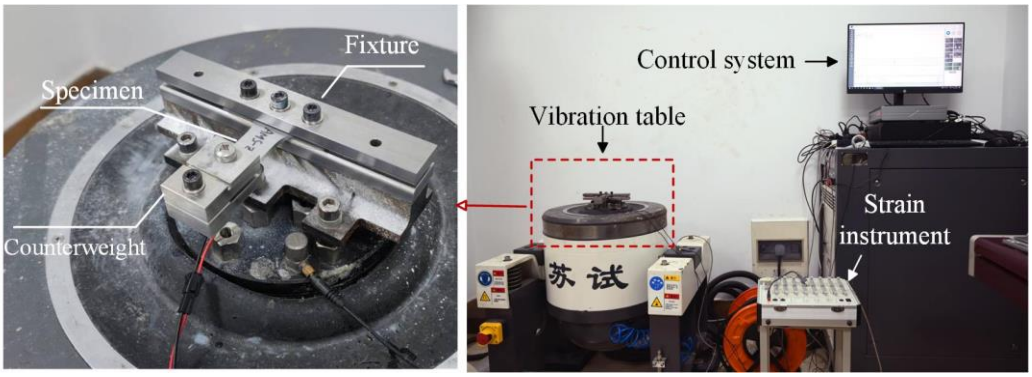

Fig.8 Fatigue testing setup

（2）Test Results

All experimental results are summarized in Table 5, where the mean values and variances were calculated assuming that the fatigue life follows a lognormal distribution. The fatigue test results indicate that the fatigue life decreases markedly with increasing loading level. For each prescribed loading spectrum, five specimens were tested. Except for the STB-2 loading spectrum, the coefficients of variation for all specimen groups are within 10%.

The coefficient of variation for the STB-2 group reaches 46%, which can be explained from two perspectives. First, STB-2 corresponds to the highest loading level applied to the TiB_2 specimens, resulting in the shortest fatigue lives among all test groups, with magnitudes on the order of only several minutes. When the overall fatigue life scale is reduced to such a short duration, deviations of individual specimens from the mean value become more pronounced. Second, materials manufactured by the SLM process inherently contain a large number of internal microporosity defects. Previous studies have demonstrated that vibration fatigue life is directly correlated with pore size [24]. The significant scatter in pore size distribution further contributes to the observed dispersion in fatigue life.

Table 5 Vibration fatigue test results

Materials	Spectrum	$m/(g^2 \cdot \mathrm{Hz}^{-1})$	Fatigue life /min					Mean value/min	Coefficient of variation /%
TiB_2	STB-0	0.05	460	220	480	400	417	377.3	6.1
	STB-1	0.1	50.0	25.0	25.0	27.5	29.5	31.8	9.0
	STB-2	0.2	9.0	8.9	6.2	5.0	1.8	5.2	46.0
TC4	STC-0	0.6	39	53	50	63	50	50.0	4.4
	STC-1	0.8	14	20	21	20.5	19	18.7	5.7
	STC-2	1.0	11	9	13	11	9	10.5	6.6

According to the results in Table 5, the fatigue life ranges corresponding to STB-0, 1, and 2 load levels are on the order of 10^6, 10^5, and 10^4 cycles, respectively, while those for STC-0, 1, and 2 are approximately 10^5, 10^5, and 10^4 cycles. These ranges fall within the high-cycle fatigue (HCF) regime and do not fully cover the transition to very-high-cycle fatigue (VHCF). Nevertheless, the selected load levels remain sufficient for validation purposes. This is because the response stress under random vibration is not a deterministic value but follows a probability distribution, with the corresponding fatigue life spanning the interval $(0, +\infty)$, as

illustrated in Fig. 9. Fatigue damage evaluation requires the complete S–N curve (Eq. (2)). For higher response stress, damage is dominated by the HCF regime, whereas for lower response stress, the contribution of VHCF damage becomes more significant. Therefore, random vibration inherently spans fatigue regimes from low-cycle to VHCF, with the relative contribution of each regime governed by stress severity.

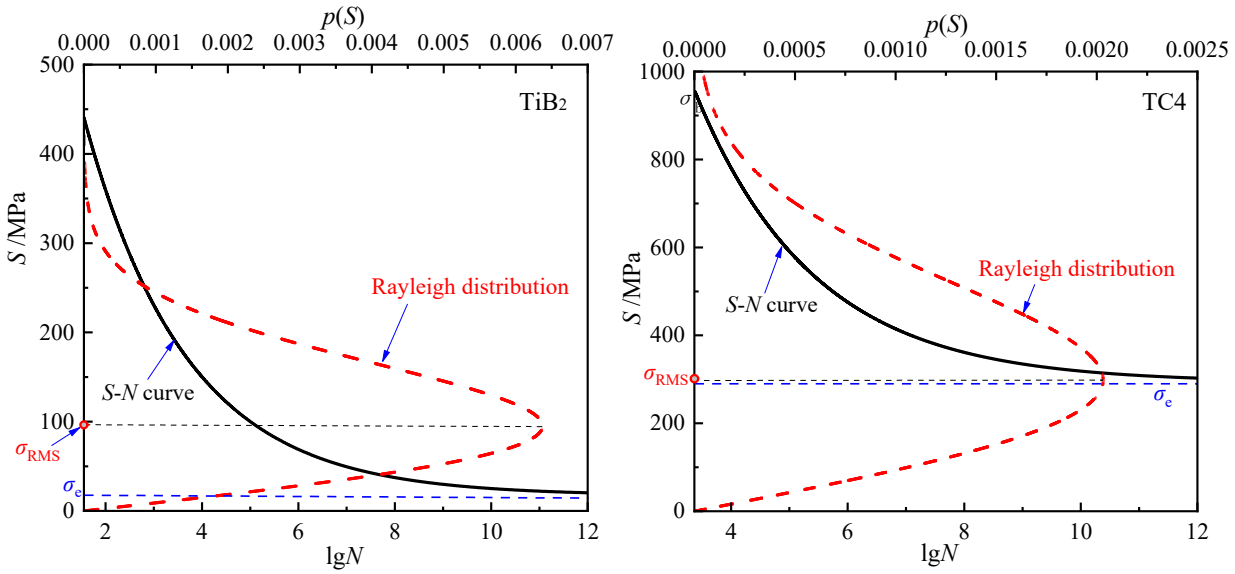

Fig. 9 Relation between the response stress amplitude distribution and the material's S-N curve

Fracture was consistently observed to occur in the transition region. Taking the line connecting the center of the arc and one end of the arc as the reference line, the arc angle was measured from this reference to the crack initiation point along the transition region. The crack initiation angles on the upper and lower surfaces are denoted by θ_1 and θ_2, respectively. Experimental observations showed that both θ_1 and θ_2 were distributed within the range of 0~15°, as illustrated in Fig.10. A detailed statistical distribution of crack initiation angles for both types of specimens is also presented in Fig.10.

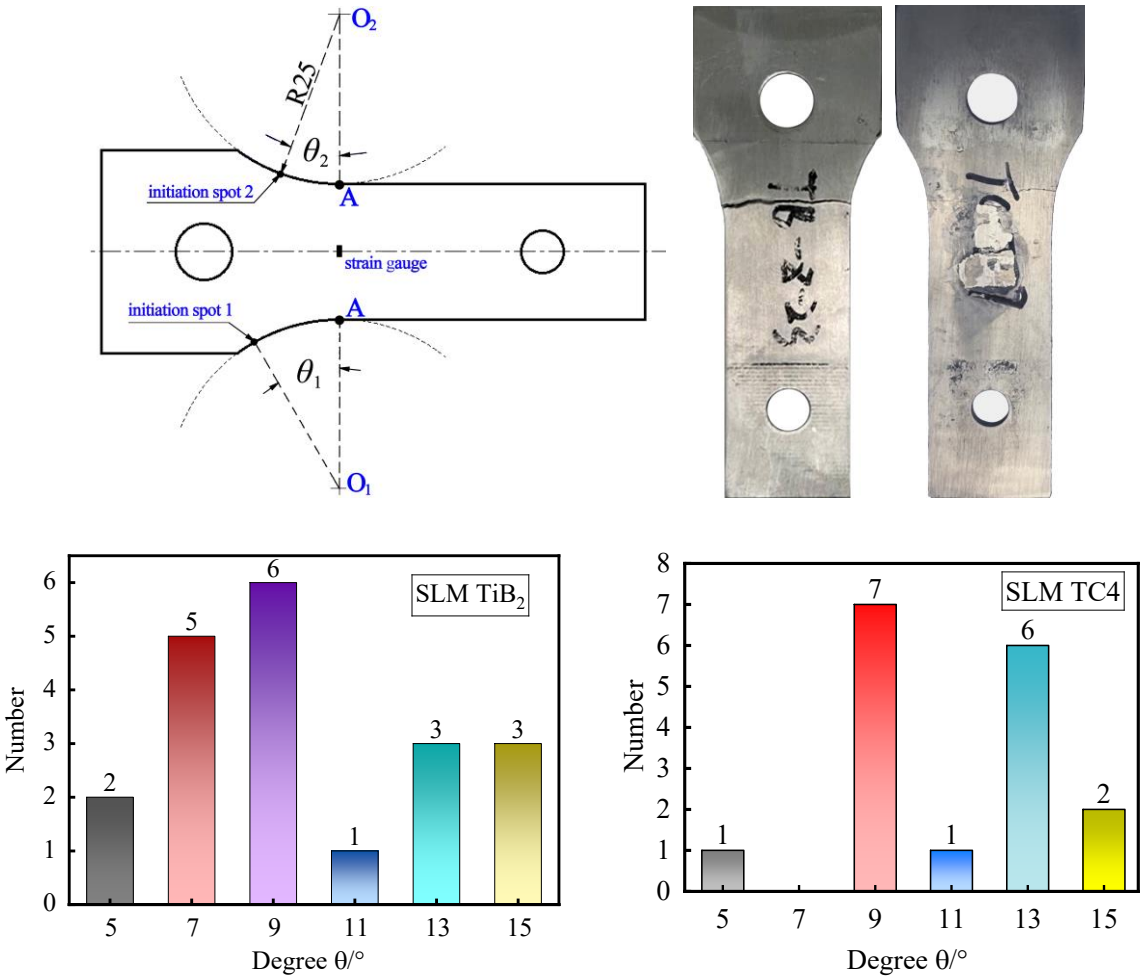

Fig. 10 Fracture angles of specimens

(3) Finite Element Analysis

Finite element analysis was employed to assist in evaluating the stress at the critical locations. A random vibration finite element model of the specimen was established, as shown in Fig.11. The FEA result at point A is represented by the maximum root-mean-square (RMS) stress, denoted as $\sigma_{\mathrm{RMS,A}}$. Point B corresponds to the location where the strain gauge was bonded, and the experimentally measured RMS stress at this point is denoted as $\sigma_{\mathrm{RMS,B}}$. The values of $\sigma_{\mathrm{RMS,A}}$, $\sigma_{\mathrm{RMS,B}}$, and their ratio are listed in Table 6. It can be observed that although the response stress levels vary under different excitation intensities, the ratio $\sigma_{\mathrm{RMS,A}}/\sigma_{\mathrm{RMS,B}}$ remains approximately constant at 1.22. This ratio is governed solely by the specimen geometry and is independent of the excitation level.

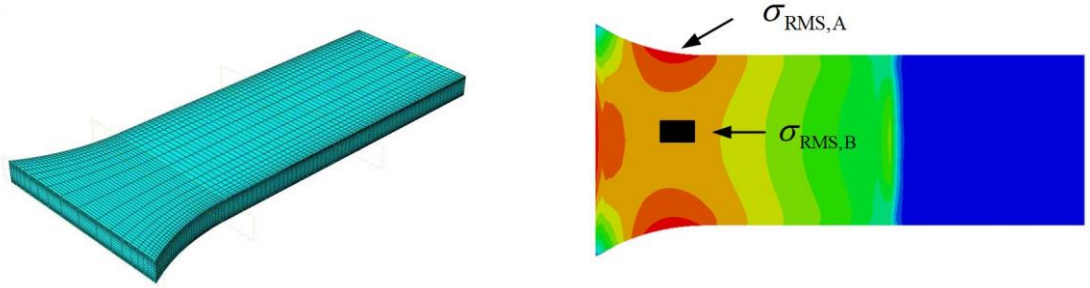

Fig.11 Finite element analysis

Table 6 FEA results of response stress $\sigma_{\mathrm{RMS\,A}}$ and $\sigma_{\mathrm{RMS\,B}}$ under different levels of excitation

Specimens	m /(g²/Hz)	$\sigma_{\mathrm{RMS\,B}}$ / MPa	$\sigma_{\mathrm{RMS\,A}}$ / MPa	$\sigma_{\mathrm{RMS\,A}}/\sigma_{\mathrm{RMS\,B}}$
TB-#	0.20	110.13	134.61	1.22
	0.10	77.58	95.18	1.23
	0.05	54.85	67.30	1.23
TC-#	1.00	271.80	333.84	1.23
	0.60	211.03	258.46	1.22
	0.30	148.87	182.85	1.23

4. Results and Discussion

4.1 Results

The experimental acceleration factor η_{test} was obtained from the fatigue life data listed in Table 5, while the predicted acceleration factor η_{predict} was calculated using Eq. (22). In this equation, $\kappa(b)=1.1608b+0.6418$, and the fatigue exponent b was taken as 4.87 for the TiB_2 alloy and 4.68 for the TC4 alloy. The values of η_{test} and η_{predict} using two-parameter S-N curve and three-parameter S-N curve are separately summarized in Table 7(a) and Table 7(b). The results are also presented in comparison with the material S-N curves in Fig 11. It should be noted that the excitation spectrum STB-0 corresponds to the baseline loading condition, whereas the acceleration factors obtained under STB-1 and STB-2 are defined as the ratios of fatigue life under these accelerated spectra to that under the baseline spectrum STB-0.

Table 7a The comparison of the acceleration factors between test and prediction (Two-parameter S-N curve)

Specimens	Stress spectra	$m/(g^2\cdot \mathrm{Hz}^{-1})$	$\sigma_{\mathrm{RMS\,A}}$ / MPa	Average test life/min	Acceleration factor η		Error/%
					test	prediction	
TB-#	STB-0	0.05	67.30	377.3	—	—	—
	STB-1	0.1	95.18	31.8	11.86	8.43	-28.92
	STB-2	0.2	134.61	5.2	72.56	71.14	-1.96
TC-#	STC-0	0.6	258.46	50.0	—	—	—
	STC-1	0.8	298.59	18.7	2.67	3.90	46.08
	STC-2	1.0	333.84	10.5	4.76	11.17	134.69

Table 7b The comparison of the acceleration factors between test and prediction (Three-parameter S-N curve)

Specimens	Stress spectra	$m/(g^2\cdot \mathrm{Hz}^{-1})$	$\sigma_{\mathrm{RMS\,A}}$ / MPa	Average test life/min	Acceleration factor η		Error/%
					test	prediction	
TB-#	STB-0	0.05	67.30	377.3	—	—	—
	STB-1	0.1	95.18	31.8	11.86	8.86	-25.33
	STB-2	0.2	134.61	5.2	72.56	78.55	8.26
TC-#	STC-0	0.6	258.46	50.0	—	—	—
	STC-1	0.8	298.59	18.7	2.67	2.48	-7.19
	STC-2	1.0	333.84	10.5	4.76	5.01	5.21

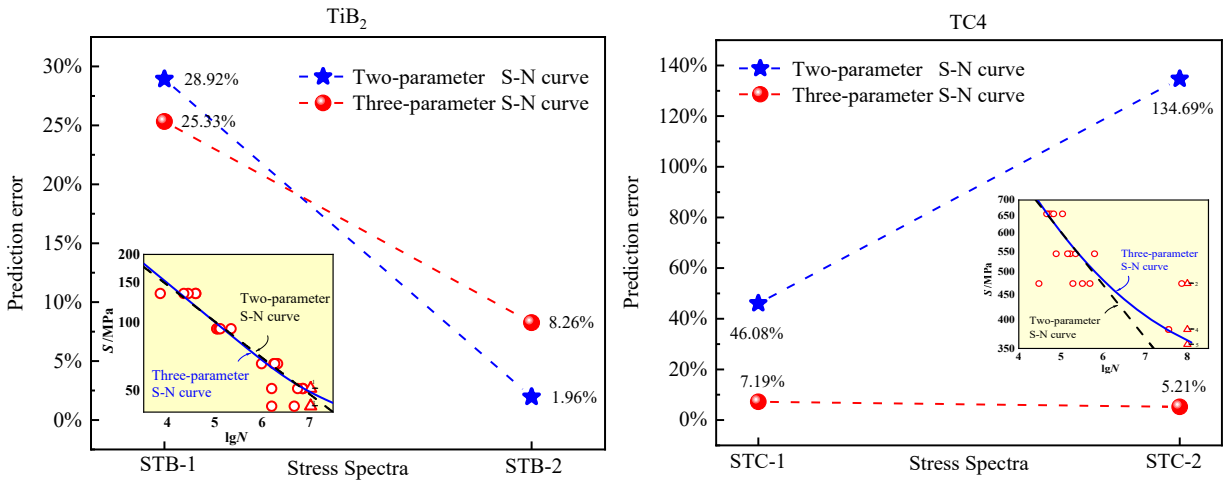

Fig.12 Comparison of absolute prediction errors with two- and three-parameter S-N curves

Table 7(a) and Fig. 12 compare the predicted acceleration factors based on the two-parameter S–N curve with experimental results. For TiB_2, the prediction errors at two load levels are −28.92% and −1.96%, respectively. In contrast, significantly larger errors are observed for TC4, reaching 46.08% and 134.69%. These results indicate that the two-parameter S–N curve adequately characterizes the fatigue behavior of TiB_2 but fails to accurately represent that of TC4. This discrepancy is consistent with the differences in S–N curve formulations (two-parameter versus three-parameter). As shown in Fig. 5, the two-parameter and three-parameter S–N curves for TiB_2 are nearly identical, even in the HCF regime (beyond 10^6 cycles), leading to comparable prediction accuracy. Conversely, for TC4, significant deviations between the two formulations emerge beyond 10^6 cycles, resulting in substantial prediction errors when using the two-parameter model.

Table 7(b) and Fig. 12 further present comparisons based on the three-parameter S–N curve. For TiB_2, the prediction errors are −25.33% and 8.26%, confirming that the choice between two- and three-parameter models has minimal impact due to their similarity. In contrast, for TC4, the prediction accuracy is significantly improved, with errors reduced from 46.08% to −7.19% and from 134.69% to 5.21%. This demonstrates that the three-parameter S–N curve substantially enhances the predictive capability for TC4. As indicated in Fig. 5, the improved accuracy arises from the more precise representation of fatigue behavior provided by the three-parameter model.

4.2 Discussion

The present study successfully established a high-precision analytical model for vibration fatigue acceleration factor based on the three-parameter S-N curve, and its validity was confirmed through experimental tests on SLM-manufactured specimens. The findings and their implications are discussed as follows.

(1) Superiority of the three-parameter S-N curve model

The introduction of the three-parameter S-N curve addresses a fundamental limitation of the traditional two-parameter model: its inability to account for the fatigue limit of materials in the high-cycle regime. In vibration fatigue, where the majority of stress cycles occur at low amplitudes near or below the fatigue limit, this omission leads to significant overestimation of cumulative damage and thus over-conservative or, in some

cases, non-conservative life predictions. The three-parameter model, by incorporating the endurance limit, provides a more physically realistic description of material behavior, particularly under high-cycle random loading. This is evidenced by the sound agreement between predicted and experimental fatigue lives observed in this study.

(2) Physical interpretation of the generalized inverse power law

The derived closed-form solution for the acceleration factor, expressed as a generalized inverse power law, offers not only computational efficiency but also valuable physical insight. The exponent $\kappa(b)$ in this law is shown to be governed by the material's S-N curve exponent b and the probability density function $p(S)$ of the stress response. This result underscores that the acceleration relationship is not an empirical fitting parameter but is intrinsically linked to the material's fatigue resistance and the statistical nature of the dynamic loading environment. The specific case where $p(S)$ is a Rayleigh function—common in stationary narrow-band Gaussian random vibrations—yields $\kappa(b)$ as a linear function of exponent b. This elegant simplification provides a powerful and straightforward tool for engineers, enabling quick yet accurate assessment of test acceleration factors for a broad class of vibration problems.

(3) Limitations and future work

In the derivation of the exponent $\kappa(b)$ in the generalized inverse power-law model, a first-order approximation is employed (Fig. 4), which effectively eliminates the explicit influence of the fatigue limit S_e in the final formulation. While the fatigue limit plays a significant role in absolute life prediction, it cancels out in relative life calculations—such as the acceleration factor, defined as the ratio of fatigue lives under different stress levels—and thus does not appear explicitly in the final expression. The influence of the three-parameter S–N curve is therefore reflected indirectly through its functional form. Notably, the exponent in the acceleration factor is inherently a multivariable nonlinear function. Although the first-order approximation facilitates engineering application, it inevitably introduces prediction errors. Refinement of this approximation constitutes an important direction for future research.

In addition, while the proposed model demonstrates high accuracy under narrow-band random vibration with Rayleigh-distributed stresses, its performance under broader-band or non-stationary loading conditions warrants further investigation. Future work could explore the extension of the model to multi-modal vibration or non-Gaussian load spectra. Additionally, the model assumes linear cumulative damage (Miner's rule). Investigating the integration of more sophisticated non-linear damage accumulation theories with the three-parameter framework could be a fruitful direction for enhancing prediction capabilities for complex load histories. Experimental verification across a wider range of materials, including composites and other advanced alloys, would further solidify the model's general applicability.

5. Conclusion

This study has systematically addressed the inherent limitations of traditional vibration fatigue acceleration testing methods by introducing a more physically accurate modeling framework. The primary conclusions can be summarized as follows:

(1) The conventional two-parameter power-law S-N curve, which fails to characterize the genuine fatigue limit of materials in the high-cycle regime, introduces a systematic and often non-conservative bias in long-term life predictions, particularly critical for vibration-dominated, high-cycle fatigue failures. The proposed adoption of the three-parameter power-law S-N curve fundamentally enhances the physical fidelity of the fatigue damage model by introducing a more accurate life formulation in the high-cycle fatigue regime.

(2) For structures subjected to narrow-band random vibration excitation, a novel and high-precision analytical model for the vibration fatigue acceleration factor has been successfully developed based on the three-parameter S-N curve. The core theoretical achievement is the derivation of a closed-form solution expressed as a generalized inverse power law. This model provides a direct and practical engineering formula for acceleration factor calculation.

(3) Within this framework, the acceleration factor is governed by the generalized inverse power law model. Its exponent, $\kappa(b)$, is determined by two factors: the material's S-N curve and the probability density function $p(S)$ of the stress amplitude response. This establishes a clear and direct link between material properties, excitation characteristics, and test acceleration. When the stress response follows a Rayleigh distribution, the exponent $\kappa(b)$ simplifies to a linear function of the S-N curve exponent b. This provides an exceptionally simple yet powerful tool for engineering applications involving stationary Gaussian random vibrations.

(4) The proposed analytical model was rigorously validated through a series of accelerated vibration fatigue tests conducted on selective laser melting fabricated aluminum and titanium alloy specimens. The results indicate that when a significant discrepancy exists between the two-parameter and three-parameter S–N curves of a material, adopting the more accurate three-parameter S–N curve can substantially improve the prediction accuracy of the vibration fatigue acceleration factor, thereby demonstrating the necessity and effectiveness of the present theoretical study.

Declaration of Competing Interest

The authors declare that they have no known competing financial interests or personal relationships that could have appeared to influence the work reported in this paper.

Acknowledgement

The authors gratefully acknowledge the financial support of the National Natural Science Foundation of China (12502395, U24A2005), Jiangsu Province Key Laboratory of Aerospace Power System（No. CEPE2025004）.

References

[1] Department of Defense, MIL-STD-810F, Environmental engineering considerations and laboratory methods, Department of Defense, United States, 2000.

[2] C.Y. Ge, Z.Z. Xu, K.F. Du, et al., An improved inverse power law model for accelerated fatigue life prediction of 6061-T6 and AZ31B-F, Eng. Fail. Anal. 138 (2022) 106381.

https://doi.org/10.1016/j.engfailanal.2022.106381.

[3] C.R. Farrar, T.A. Duffey, P.J. Cornwell, et al., A review of methods for developing accelerated testing criteria, Proc. 17th Int. Modal Anal. Conf., Kissimmee, FL, 1999, pp. 608–614.

[4] L. Xu, G.Z. Dai, Accelerated life test and FEM simulation-based fatigue analysis of an aluminum alloy push rod, Strength Mater. 51 (2019) 32–39. https://doi.org/10.1007/s11223-019-00047-y.

[5] S.B. Ameur, M. Mtibaa, A. Yaich, et al., A complete approach for evaluating the vibrational behavior of RTM-manufactured functional composites under random vibrations, Compos. Commun. 58 (2025) 102530. https://doi.org/10.1016/j.coco.2025.102530.

[6] A.V.A. Dupke, É. Pessard, D. Mellé, A. Ross, M. Brochu, Novel high cycle vibration-based fatigue test for pure shear loading, Int. J. Fatigue 202 (2026) 109180. https://doi.org/10.1016/j.ijfatigue.2025.109180.

[7] G. Allegri, X. Zhang, On the inverse power laws for accelerated random fatigue testing, Int. J. Fatigue 30 (2008) 967–977. https://doi.org/10.1016/j.ijfatigue.2007.08.023.

[8] D. Benasciutti, Some analytical expressions to measure the accuracy of the “equivalent von Mises stress” in vibration multiaxial fatigue, J. Sound Vib. 333 (2014) 4326–4340. https://doi.org/10.1016/j.jsv.2014.04.047.

[9] C.J. Kim, Accelerated sine-on-random vibration test method of ground vehicle components over conventional single mode excitation, Appl. Sci. 7 (2017) 805. https://doi.org/10.3390/app7080805.

[10] Y. Jiang, J.Y. Tao, Y.A. Zhang, G.J. Yun, Fatigue life prediction model for accelerated testing of electronic components under non-Gaussian random vibration excitations, Microelectron. Reliab. 64 (2016) 120–124. https://doi.org/10.1016/j.microrel.2016.07.018.

[11] Y. Wang, R. Serra, P. Argoul, Adapted Locati method used for accelerated fatigue test under random loading, Procedia Struct. Integr. 19 (2019) 674–681. https://doi.org/10.1016/j.prostr.2019.12.073.

[12] W. Lei, Y. Jiang, X. Zeng, Z. Fan, A novel excitation signal generation technology for accelerated random vibration fatigue testing based on the law of kurtosis transmission, Int. J. Fatigue 159 (2022) 106835. https://doi.org/10.1016/j.ijfatigue.2022.106835.

[13] M. Česnik, J. Slavič, M. Boltežar, Accelerated vibration-fatigue characterization for 3D-printed structures: Application to fused-filament-fabricated PLA samples, Int. J. Fatigue 171 (2023) 107574. https://doi.org/10.1016/j.ijfatigue.2023.107574.

[14] C. Ge, Z. Song, C. Zhou, H. Guo, D. Zhu, B. Wang, A novel accelerated fatigue test method of mission synthesis considering the segmented S-N curve, Int. J. Fatigue 193 (2025) 108789. https://doi.org/10.1016/j.ijfatigue.2024.108789.

[15] S. Ozsoy, M. Celik, F.S. Kadioglu, An accelerated life test approach for aerospace structural components, Eng. Fail. Anal. 15 (2008) 946–957. https://doi.org/10.1016/j.engfailanal.2007.10.015.

[16] A. Pothula, A. Gupta, G.R. Kathawate, Fatigue failure in random vibration and accelerated testing, J. Vib. Control 18 (2012) 1199–1206. https://doi.org/10.1177/1077546311419545.

[17] A. Angeli, B. Cornelis, M. Tronc, Synthesis of sine-on-random vibration profiles for accelerated life tests based on fatigue damage spectrum equivalence, Mech. Syst. Signal Process. 103 (2018) 340–351. https://doi.org/10.1016/j.ymssp.2017.10.022.

[18] C. Wen, B. Xie, Z. Li, Y. Yin, X. Zhao, Z. Song, Power density based fatigue load spectrum editing for accelerated durability testing for tractor front axles, Biosyst. Eng. 200 (2020) 73–88. https://doi.org/10.1016/j.biosystemseng.2020.09.008.

[19] M. Kepka, M. Kepka Jr., Accelerated fatigue testing on special tracks as new part of methodology for bus/trolleybus development, Eng. Fail. Anal. 118 (2020) 104786. https://doi.org/10.1016/j.engfailanal.2020.104786.

[20] G. D'Elia, E. Mucchi, G. Dalpiaz, A novel methodology for dynamic response maximisation in multi-axis accelerated random fatigue testing, Mech. Syst. Signal Process. 181 (2022) 109491. https://doi.org/10.1016/j.ymssp.2022.109491.

[21] J.H. Lee, H.Y. Cho, An experimental study of the lifetime of a tripod shaft with torsional fatigue using an accelerated life test method, Int. J. Precis. Eng. Manuf. 19 (2018) 1399–1404. https://doi.org/10.1007/s12541-018-0165-1.

[22] Y. Zhu, P. Li, A tail probability density distribution model of stress amplitude under band-limited stochastic vibration loadings, Proc. Inst. Mech. Eng. G: J. Aerosp. Eng. 239 (2025) 136–148. https://doi.org/10.1177/09544100241287666.

[23] W. Yao, Fatigue Life Estimation of Structures, Science Press, Beijing, 2019.

[24] Y. Yang, H. Yin, P. Li, D. Fu, W. Yao, Defect extreme value analysis and fatigue life prediction model for SLM-manufactured TiB2-Al and TC4 alloys, Eng. Fail. Anal. 170 (2025) 109244. https://doi.org/10.1016/j.engfailanal.2024.109244.